



Construction of hierarchical 2D-2D $\text{Zn}_3\text{In}_2\text{S}_6$ /fluorinated polymeric carbon nitride nanosheets photocatalyst for boosting photocatalytic degradation and hydrogen production performance

Yan Wu^a, Hou Wang^{a,**}, Wenguang Tu^a, Yue Liu^a, Shuyang Wu^a, Yong Zen Tan^a,
Jia Wei Chew^{a,b,*}

^a School of Chemical and Biomedical Engineering, Nanyang Technological University, 637459, Singapore

^b Singapore Membrane Technology Center, Nanyang Environment and Water Research Institute, Nanyang Technological University, 639798, Singapore

ARTICLE INFO

Keywords:

$\text{Zn}_3\text{In}_2\text{S}_6$ nanosheets
Polymeric carbon nitride
Fluorine doping
Photocatalytic degradation
Photocatalytic hydrogen generation

ABSTRACT

The development of novel hybrid photocatalysts with high efficiency and durability for photocatalytic degradation and hydrogen production is highly desired, but still remains a great challenge currently. In this work, novel hierarchical composites consisting of petal-like $\text{Zn}_3\text{In}_2\text{S}_6$ nanosheets and varying amounts of fluorine doped polymeric carbon nitride (FCN) were successfully prepared as photocatalysts for the photocatalytic degradation of methyl orange and H_2 evolution under visible light irradiation. The incorporation of FCN into $\text{Zn}_3\text{In}_2\text{S}_6$ nanosheets significantly enhanced the photocatalytic activity for H_2 evolution (reduction) and degradation of methyl orange (oxidation). And the best-performing $\text{Zn}_3\text{In}_2\text{S}_6$ /FCN composite (i.e., ZF3) exhibited enhanced visible-light-driven photocatalytic methyl orange degradation efficiency of about 7.36 and 5.35 times higher than those of pure FCN and $\text{Zn}_3\text{In}_2\text{S}_6$, respectively. Trapping experiments combined with electron spin resonance spectroscopy indicated that the active radicals ($\cdot\text{O}_2^-$ and $\cdot\text{OH}$) and oxidizing h^+ were responsible for the photocatalytic reaction. Meanwhile, the cumulative H_2 evolution quantity by ZF3 sample via photocatalytic H_2 evolution from water splitting under 5 h of light irradiation reached $2553.9 \mu\text{mol.g}^{-1}$, which was 3.66 times higher than that of $\text{Zn}_3\text{In}_2\text{S}_6$ ($698.2 \mu\text{mol.g}^{-1}$). Cyclic tests demonstrated the stability of the ZF3 composite over five cycles of repeated use. These excellent performances were found to be attributable to the remarkable charge carrier separation between FCN and $\text{Zn}_3\text{In}_2\text{S}_6$, with the aid of interfacial heterojunction structures. Based on the above results, the possible photocatalytic reaction mechanisms of ZF3 composite in both pollutant degradation and H_2 evolution from water splitting were also proposed. This study provides new insights into the preparation of highly-efficient hierarchical composite photocatalysts, which are promising for implementation in wide-ranging environmental applications.

1. Introduction

Photocatalysis is well-acknowledged as an effective method for the abatement of aqueous pollutants in wastewater treatment and environmental remediation. Various semiconductor photocatalysts have been employed in this regard in the last few years [1–3]. Recently, as a new and important member in the community of ternary chalcogenides, Zn-In-S (the general formula is $\text{Zn}_m\text{In}_{2-3+m}\text{S}_{3+m}$, $m = 1-5$) is of increasing interest to applications such as energy conversion and photocatalysis due to its unique electronic structure, appropriate band gaps and band edges, as well as tunable optical properties [4]. The configuration of two-dimensional (2D) nanosheets is favorable to reduce the diffusion

length of charge carriers, provide high surface area and expose abundant catalytically active sites for heterogeneous photocatalysis. For example, hierarchical ZnIn_2S_4 sub-microspheres delivered a high photocatalytic H_2 production under visible light exposure [5]. In solar-driven CO_2 reduction, the one-unit-cell ZnIn_2S_4 layers with rich zinc vacancies showed a CO formation rate of $33.2 \mu\text{mol.g}^{-1}\text{h}^{-1}$ [6]. Various modified methods including doping [7], morphology modulation [8] and integration with other components [9–11] have also been adopted to enhance the photocatalytic activity of ZnIn_2S_4 . However, there is still relatively less attention for other ternary chalcogenides such as $\text{Zn}_3\text{In}_2\text{S}_6$.

Poulios and Papadopoulos firstly demonstrated that n-type $\text{Zn}_3\text{In}_2\text{S}_6$

* Corresponding author at: School of Chemical and Biomedical Engineering, Nanyang Technological University, Singapore 637459, Singapore.

** Corresponding author.

E-mail addresses: huankewanghou024@163.com (H. Wang), JChew@ntu.edu.sg (J.W. Chew).

semiconductor with the band gap energy of 2.81 eV had good photoelectrochemical behavior [12]. Song et al. investigated the color-adjustable luminophores of $\text{Zn}_3\text{In}_2\text{S}_6$ quantum dots originated from shallow donor–acceptor (D–A) pair recombination and intrinsic trap state-related deep D–A pair transition [13]. Very recently, Zhang et al. developed a $\text{Zn}_3\text{In}_2\text{S}_6/\text{ZnO}$ photothermocatalyst, which showed enhanced activity, relative to $\text{Zn}_3\text{In}_2\text{S}_6$ or ZnO alone, for the selective oxidation of benzyl alcohol to benzaldehyde [14]. Despite these progresses, the catalytic performance of single ternary chalcogenides photocatalysts especially for $\text{Zn}_3\text{In}_2\text{S}_6$ is not satisfactory, mainly due to the sluggish separation and migration kinetics of charge carriers. Heterogeneous coupling of stable and efficient non-metal semiconductors with suitable band gap potentials is expected to be a strategy to improve the performance of photocatalysts, because the existence of a built-in potential gradient between the nanosized interfaces can speed up separation and transfer of electron–hole pairs and ameliorate photostability of hybrid materials simultaneously.

Polymeric carbon nitride (CN) materials with facile synthesis procedures, apt electronic band structures (~ 2.7 eV), high physicochemical stability, is a promising metal-free semiconductor photocatalyst in several applications such as solar energy conversion and wastewater treatment [15–18]. Element doping can tune the electronic structure and band gap of CN for broadening the light-responsive range, enhancing charge separation and transportation, and prolonging the charge carrier lifetime [19–21]. Previous experimental studies demonstrated that non-metal element doping, such as doping with P, B, C, O, and S, is an effective way to enhance the photocatalytic performance of g- C_3N_4 [22–28]. Wang et al demonstrated that the incorporation of F at the bay carbon of C_3N_4 shifts both LUMO and HOMO to higher energy values; however, incorporation of F at the corner carbon shifts the LUMO to higher energy and the HOMO to lower energy values. This remarkable LUMO and HOMO energy changes brought by fluorine doping are expected to modify the redox properties and promote heterogeneous photocatalysis [29]. For the synthesis method, Ma et al. developed a one-step route to simultaneously exfoliate and fluorinate CN nanosheets (FCN) using bulk g- C_3N_4 powder combined with ammonium fluoride (NH_4F) [30].

Inspired by these fascinating ideas, the coupling of $\text{Zn}_3\text{In}_2\text{S}_6$ with fluorinated polymeric carbon nitride nanosheets with hierarchical structure is expected to improve the separation efficiency of the photogenerated electrons–holes via the interfacial contact due to the well-matched valence band and conduction band edge potentials [31]. Moreover, the designed and unique 2D/2D structure has much more contact areas, and shorter migration distance and time for photo-induced charges, which favors the high-speed charge transfer along the expected migration route (from $\text{Zn}_3\text{In}_2\text{S}_6$ nanosheet to the intimate heterojunction interface then to FCN nanosheet). Accordingly, this kind of composites can be efficient, visible-light-responsive and stable photocatalysts for solar energy conversion and pollutant removal. However, to the best of our knowledge, there is no report on the fabrication of hierarchical 2D-2D $\text{Zn}_3\text{In}_2\text{S}_6$ /fluorinated polymeric carbon nitride nanosheets composites, and the corresponding application in hydrogen generation and environmental remediation.

In this study, an in-situ fabrication of $\text{Zn}_3\text{In}_2\text{S}_6$ /FCN photocatalysts with different exfoliated FCN content had been carried out through the one-pot solvothermal method. When integrating $\text{Zn}_3\text{In}_2\text{S}_6$ nanostructure with FCN nanosheets, a significant enhancement on photocatalytic H_2 production and methyl orange photodegradation could be obtained through synergistic promotion of the inner charge carriers and outer hierarchical structures. Furthermore, the intimate contact interface between the $\text{Zn}_3\text{In}_2\text{S}_6$ and FCN nanosheets facilitated the photo-induced charge-carrier transfer from FCN to $\text{Zn}_3\text{In}_2\text{S}_6$ based on the heterojunction effect. The underlying mechanisms were explored by using photoluminescence spectroscopy, photocurrent-time measurement, active species trapping experiments and electron spin resonance (ESR) analysis. The results here are expected to be valuable for

potential applications in the water purification and hydrogen energy conversion fields.

2. Experimental

2.1. Material synthesis

All reagents were of analytical grade from Sigma-Aldrich, and used as received without further purification. Deionized water was used in the synthesis.

2.1.1. Synthesis of polymeric carbon nitride (CN)

The CN sample was obtained by a facile thermal polymerization method [32]. In brief, 10 g melamine was placed in an alumina crucible and heated in air atmosphere at 400 °C for 2 h at 3 °C/min, then 550 °C for 2 h at 5 °C/min, and finally left to naturally cool to room temperature.

2.1.2. Synthesis of fluorine-doped polymeric carbon nitride (FCN)

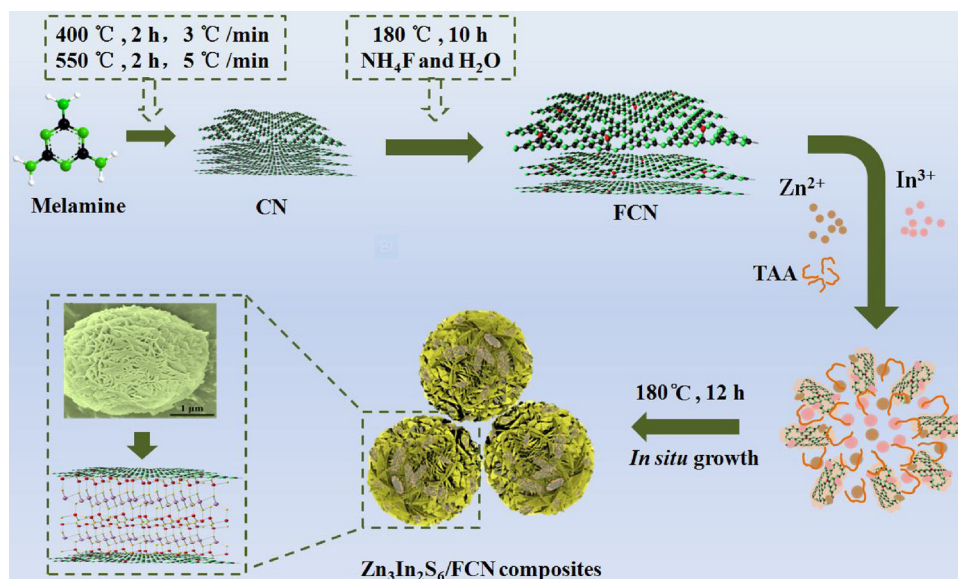
In a typical experiment, CN (0.5 g) and ammonium fluoride (2 g) were further ground into a homogeneous form and transferred into a Teflon-lined stainless steel autoclave. Deionized water (40 mL) was added and the system was heated at 180 °C for 10 h, and then cooled down to room temperature. The autoclave container was taken out, and the product was centrifuged and washed with ethanol and deionized water repeatedly until the pH of the supernatant was close to neutral. Finally, the samples were dried in a vacuum oven for 12 h.

2.1.3. Synthesis of $\text{Zn}_3\text{In}_2\text{S}_6$ /FCN composite (ZF)

In a typical synthesis, 2 mmol $\text{In}(\text{NO}_3)_3 \cdot 6\text{H}_2\text{O}$, 3 mmol ZnCl_2 and a double excess of thioacetamide were dissolved in 40 mL of deionized water. Then the targeted amount of FCN was added and sonication continued for 30 min, followed by 2 h of magnetic stirring. Specifically, the mass of FCN added was either 10, 30, 50 or 80 mg during the synthesis process, with the resulting hybrids denoted by ZF1, ZF3, ZF5 and ZF8, respectively. The mixed solution was transferred into a Teflon-lined stainless-steel autoclave and kept at 180 °C for 12 h in an electric oven. After cooling to room temperature naturally, the products were collected by centrifugation, washed with ethanol and distilled water several times, and finally dried in an electric oven at 60 °C for 10 h. The synthesis procedure for $\text{Zn}_3\text{In}_2\text{S}_6$ (ZIS) nanosheet is the same as that for ZF composite synthesis but without the addition of FCN into the starting reaction mixture. The overall procedure of the preparation of the ZF photocatalyst is depicted in the Scheme 1.

2.2. Characterization methods

Transmission electron microscope (TEM) images were obtained using the JEOL 2010 HR & UHR (Japan) operated at an accelerating voltage of 100 kV. The freshly prepared sample was dispersed by ultrasound before characterization. Scanning electron microscope (SEM) images were obtained using the JEOL JSM 6700 F (Japan) in different magnifications at an accelerating voltage of 15 kV. UV–vis diffuse-reflectance spectra (UV–vis DRS) were recorded in the range of 200–800 nm with a UV-2450 spectrometer equipped with an integrating sphere. The powder X-ray diffraction (XRD) patterns were recorded using Bruker AXS D8 Advance diffractometer operating with the Cu-K α source to investigate the crystal structure of the samples. The X-ray photoelectron spectroscopy (XPS) measurements were conducted with an Axis Ultra DLD spectrometer (Kratos Analytical Ltd., England) with monochromatized Al K α X-ray source ($h\nu = 1486.6$ eV). Photoluminescence (PL) spectroscopy was measured at the excitation wavelength of 325 nm at room temperature by Perkin-Elmer LS-55 spectrofluorimeter. The time-resolved fluorescence decay spectrum was performed on an Edinburgh FLS980 spectrophotometer at an excitation wavelength of 325 nm. The electron spin resonance (ESR) signals of



Scheme 1. Schematic representation of the formation mechanism of fluorine-doped polymeric carbon nitride (FCN) and $\text{Zn}_3\text{In}_2\text{S}_6/\text{FCN}$ composite.

radicals spin-trapped by spin-trapped reagent 5, 5-dimethyl-1-pyrroline N-oxide (DMPO) and 2,2,6,6-Tetramethylpiperidinoxy (TEMPO) were examined via a Bruker ER200-SRC spectrometer under visible light irradiation ($\lambda > 420 \text{ nm}$). Photocurrent-time (PT) was tested with a CHI 660 C electrochemical station in a standard three-electrode configuration.

2.3. Photocatalytic performance test

2.3.1. Photocatalytic methyl orange (MO) solution

The photocatalytic activity of the ZF composite was evaluated by the extent of degradation of MO under visible light irradiation. A 300 W Xenon lamp with an UV cut-off filter ($\lambda > 420 \text{ nm}$) was used as a visible light source (20 V, 15 A, 15 cm away from the photocatalytic reactor). For the decomposition of MO, 40 mg of the ZF photocatalyst was dispersed in 100 mL of 10 mg/L MO aqueous solution. The solution was continuously magnetically stirred with a magnetic bar during irradiation to ensure homogeneity. Prior to the photoreaction, the suspension was magnetically stirred in the dark for 60 min to attain adsorption/desorption equilibrium. Upon irradiation, 3 mL samples were withdrawn from the suspension every 10 min for up to 60 min. After that, the ZF composite particles were removed via centrifugation (10,000 rpm for 10 min). The MO concentrations in the samples were

quantified with a UV–vis spectrophotometer at the wavelength of 463 nm (UV-2450, Shimadzu, Japan).

2.3.2. Photocatalytic H_2 evolution

The evolution of H_2 released is also an indicator of photocatalytic activity. Typically, 50 mg of the catalyst was dispersed in 100 mL aqueous solution containing 0.25 M Na_2SO_3 and 0.35 M Na_2S as sacrificial electron donor and 2 wt % $\text{H}_2\text{PtCl}_6 \cdot 6\text{H}_2\text{O}$ as a co-catalyst during the reaction. A 250 mL top-irradiation quartz reaction vessel was connected to an enclosed vitreous gas recirculation system, and a 300 W Xe lamp was used as the light source, with a cut-off filter applied to generate visible light ($\lambda > 420 \text{ nm}$). Prior to the photoreaction, the system was vacuumed to completely remove air and the dissolved oxygen. The reaction temperature was maintained at room temperature through the cooling water circulation system and the accumulated amount of evolved gases was monitored in situ every 60 min interval using a gas chromatograph equipped with a thermal conductive detector (TCD).

3. Results and discussion

3.1. Structure and morphology

The crystal structure and phase composition of the synthesized

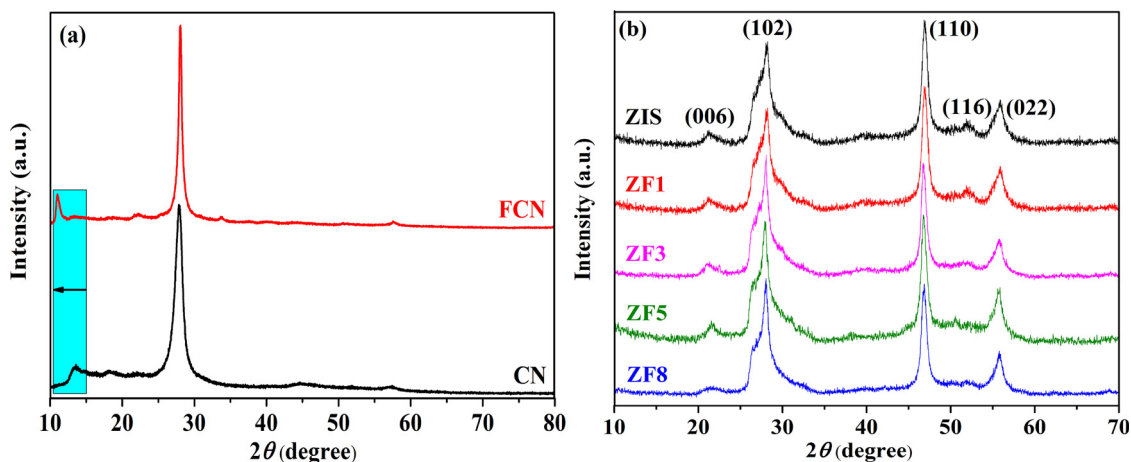


Fig. 1. XRD patterns of CN, FCN, ZIS and ZF composites.

samples were investigated by using XRD, and the representative XRD patterns of CN, FCN, ZIS and ZF composites are shown in Fig. 1(a) and (b). Fig. 1(a) reveals that both CN and FCN shared the same characteristic structure with the (002) peak at 28.08° , corresponding to the typical interlayer-stacking structure [30]. The low-angle peak shows a downshift from 13.31° for the CN to 11.03° for FCN, which suggests a larger distance of the in-planar structure packing motif and more short-range order [33]. It had been reported that the F^- ions opened the original $C=N$ bonds in CN, in which sp^2 C and sp^2 N converted respectively to sp^3 C and sp^3 N, leading to the buckling of the nanosheets. Accompanied by the fluorination process, the interlayer spacing of FCN enlarged and resulted in the exfoliation of nanosheets [30]. As shown in Fig. 1(b), the XRD pattern of ZIS can be indexed to a hexagonal phase of $Zn_3In_2S_6$ (JCPDS No. 65-4003), which is consistent with the previous report [14]. In the case of ZF composites, the XRD pattern shows diffraction peaks of both ZIS and FCN, while the feature peaks of ZIS (28.01°) and FCN (28.12°) are very close and overlap with each other. Moreover, it is notable that no other new diffraction peaks can be observed in the XRD patterns, indicating that FCN and ZIS were maintained as pure species and no impurities were formed in the ZF composites. However, the intensity of the (116) crystal plane reduced, which may be attributed to the introduction of FCN nanosheets. Similar results had been reported by Qiu et al. [34].

Fig. 2 shows the SEM images of ZIS and the ZF3 composite. As shown in Fig. 2(a), it is clear that the prepared ZIS exhibited regular microsphere-like shape with an average diameter of about 3–4 μm , and these microspheres were comprised of plentiful petals/sheets with smooth surface. When FCN was loaded on the ZIS microspheres, several small nanosheets (relatively dark area) can be found to adhere to the surface of ZIS petals (relatively white area) (Fig. 2(b)). It can be seen from Fig. 2(b) that the morphology of the ZF3 sample was also similar to that of ZIS in general, but some small nano-fragments can be found to be adhered to the surface of the petals for the former. Those fragments are believed to be FCN nanosheets, as demonstrated by the EDS element analysis. To further clarify the composition profile of the as-synthesized ZF3 composite, EDS-mapping analysis was carried out. As shown in Fig. 2, C, N and F were enriched on the entire microsphere as well as the fragments adhered on the surface of the microspheres, while Zn, In and S were distributed within the microsphere. This demonstrates that the assembled FCN nano-fragments were grown on the whole surface of the ZIS microsphere to form a composite photocatalyst.

TEM imaging was carried out to characterize the microcosmic structure of the ZF3 composite samples. Fig. 3(a)–(c) illustrate the attachment of the ultrathin FCN nanosheets to the surface of ZIS nanosheet. Fig. 3(d) presents the high-resolution TEM image of the ZF3 composite, which shows the lattice-fringe spacing of 0.32 nm belonging to the d-spacing of the (102) planes of hexagonal ZIS. When the FCN combined with the ZIS sheets, the lattice strips of the ZIS became less distinct and even blurry, indicating that the FCN nanosheets integrated compactly on the surface of the ZIS sheets to construct a well-defined sheet-on-sheet (2D-2D) heterostructure via the in-situ growth process. Combined with the XRD results in Fig. 1, such well-matched interface is expected to be advantageous for efficient interfacial charge transfer.

3.2. Chemical states

X-ray photoelectron spectroscopy (XPS) measurements have been carried out to elucidate the surface composition and chemical states of the ZF3 composite, and the results are shown in Fig. 4. The C 1s spectrum (Fig. 4(a)) of the ZF3 composite can be deconvoluted into three peaks at 284.4 eV, 287.9 eV and 289.2 eV. Specifically, the peak at 287.9 eV is identified as sp^2 -bonded carbon in N-containing aromatic rings ($N-C=N$), and the weak peak at 284.4 eV is typically ascribed to sp^2 C–C bonds [35,36]. Furthermore, a C–F peak also appeared at 289.2 eV, which provides evidence of the existence of F [37]. The XPS spectrum of F 1s can be divided into two main components due to the

presence of different F–C bond configurations (Fig. 4(b)). The F–C contribution at the lower binding energy (684.1 eV) is associated with an isolated fluorine atom forming a weak bond with a basal carbon atom, and its bond length is larger than the one associated with the covalent F–C bond (687.9 eV) [38,39]. The exact F concentration in the ZF3 composite determined by XPS analysis was 3.34 at%. As shown in Fig. 4(c), the N1s spectrum of the FCN was classified into two different peaks at 399.2 and 400.5 eV, with each peak corresponding to tertiary nitrogen $N-(C)_3$ and amino groups ($C-N-H$), respectively [40,41]. It can be seen from Fig. 4(d) that the high-resolution S 2p spectra of ZF3 has two peaks for S^{2-} at 161.2 eV ($S\ 2p_{3/2}$) and 162.4 eV ($S\ 2p_{1/2}$) [42]. As shown in Fig. 4(c), the N1s spectrum of the FCN was classified into two different peaks at 399.2 and 400.5 eV, corresponding to tertiary nitrogen $N-(C)_3$ and amino groups ($C-N-H$), respectively [40,41]. It can be seen from Fig. 4(d) that the high-resolution S 2p spectra of ZF3 has two peaks for S^{2-} at 161.2 eV ($S\ 2p_{3/2}$) and 162.4 eV ($S\ 2p_{1/2}$) [42]. However, upon the introduction of FCN onto ZIS nanosheets to form the heterojunctions, the N 1s characteristic signals of the ZF3 nanosheets shifted slightly towards higher binding energy. On the contrary, the binding energies of S 2p for the ZF3 nanosheets were a little lower than the corresponding values for the pure ZIS nanosheets. The binding energy shifts for the heterojunction components could be explained by the change of electron concentration, which resulted from the strong interaction between FCN and ZIS nanosheets via the N–S bond [43]. Thus, it is reasonable to conclude that the N–S bond between the two components provided a channel that facilitates the interfacial charge transfer during the photocatalytic process. As for the In 3d XPS spectrum (Fig. 4(e)), there are two peaks located at 444.9 eV ($In\ 3d_{5/2}$) and 452.5 eV ($In\ 3d_{3/2}$), implying that the valence state of the element indium is + 3 [44,45]. The XPS spectrum of Zn 2p in Fig. 4(f) can be divided into two separate peaks centered at 1022.1 eV and 1045.1 eV belonging to $Zn^{2+}\ 2p_{3/2}$ and $2p_{1/2}$, respectively [46]. Thus, from the SEM, TEM and XPS results, it can be inferred that ZIS has been successfully hybridized with the FCN via the formation of heterojunctions, which provide well-suited channels for the photo-induced charge transfer between two semiconductors.

3.3. Optical property

The optical absorption properties of FCN, ZIS and the ZF composites were investigated by UV–vis diffuse reflectance spectroscopy (DRS), as shown in Fig. 5(a). In particular, the ZF3 composites had absorption edges of longer wavelengths in comparison with the other ZF composites. The red shift might suggest that the ZF3 composites can absorb more visible light, which may result in the generation of more electron-hole pairs, signifying that the ZF3 composites are promising visible-light photocatalyst. Typically, the energy band-gap values of FCN, ZIS and ZF3 composites can be estimated using the Kubelka–Munk function [47]:

$$\alpha h\nu = A(h\nu - E_g)^{n/2}$$

where α , h , ν , h , E_g and A are the absorption coefficient, Planck constant, light frequency, band gap energy and a constant, respectively. As shown in Fig. 5(b), the E_g values of FCN, ZIS, and ZF1, ZF8, ZF5 and ZF3 composites were calculated to be 2.87, 2.78, 2.78, 2.77, 2.76 and 2.67 eV, respectively. The difference between the band gaps in ZIS and ZF samples is relatively small, suggesting the optical properties of $Zn_3In_2S_6$ are not apparently changed by addition of FCN. The slight discrepancy may be caused by few layered FCN nano-fragments loaded on the surface or inserted into $Zn_3In_2S_6$. Furthermore, VB-XPS was obtained to further investigate the property of the band structure, which can probe the total density of state (DOS) distribution in the valence band [48]. As shown in Fig. 5(c), the valence band maximum (VBM) of FCN and ZIS were determined to be 1.92 eV and 1.75 eV, respectively. Considering the band gap energies shown in Fig. 5(b), the

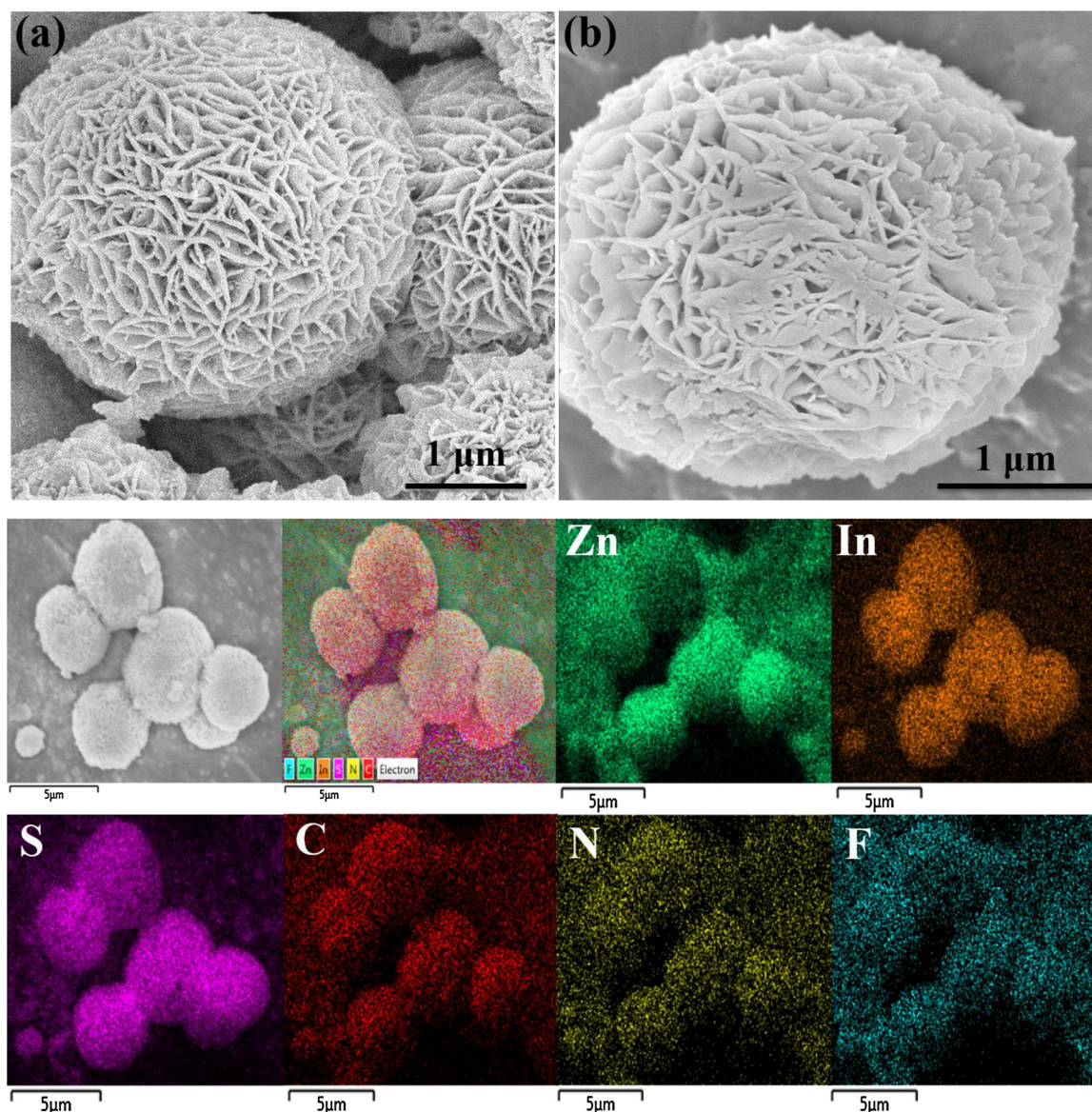


Fig. 2. SEM images of ZIS (a) and ZF3 composite (b), as well as the EDS elemental mapping analysis of the ZF3 composite.

conducting band (CB) positions of FCN and ZIS were calculated to be -0.95 eV and -1.03 eV, respectively.

The photoluminescence (PL) emission spectrum is often employed to study the surface structure and excited states, and it can provide useful information about charge carrier trapping and recombination in a semiconductor since the PL emission comes from the recombination of free charge carriers [49–51]. The higher the intensity of the PL spectra is, the faster the recombination of the electrons and holes is, and thereby the lower the photocatalytic activity is. Fig. 6 shows a comparison among the PL emission spectra of the different samples monitored at an excitation wavelength of 325 nm. It can be seen that pure ZIS exhibited a strong emission peak at around 485 nm. For ZF composites, their PL spectra were similar to that of pure ZIS, but the fluorescence peak significantly decreased. Such an obvious decrease of the fluorescence peak intensity indicates the low recombination rate of photogenerated electrons and holes in the ZF composite system. Notably, the ZF3 composite had the lowest peak magnitude, which indicates the lowest photo-generated electron–hole (e^-h^+) recombination rate and thereby implies the greatest photocatalytic activity.

The time-resolved fluorescence decay spectra provide important information about the exciton lifetime, which represents a crucial

indicator of the efficiency of the radiative recombination of the photoinduced charges. The results of the measurements are shown in Fig. 7 and summarized in the inset table. Fig. 7 shows that both the pure ZIS and ZF3 composite exhibited biexponential decay, and the fluorescence peak decay of the ZF3 composite was slower than that of ZIS. To shed light on this issue, fitting of the time-resolved transient PL spectroscopy was attempted to the multi-exponential kinetics function expressed as follows [52]:

$$I(t) = B_1 \cdot \exp(-t/\tau_1) + B_2 \cdot \exp(-t/\tau_2) \quad (1)$$

where τ_1 and τ_2 are the fluorescent lifetimes, and B_1 and B_2 are the corresponding amplitudes. As listed in the insets of Fig. 7, the smaller magnitudes of τ_1 originated from the non-radiative recombination of charge-carriers in the defect states of ZIS, while the larger magnitudes of τ_2 was caused by the free excitons recombination in the ZIS nanosheets [53,54]. In the case of ZF3 heterojunction nanosheets, τ_1 and τ_2 were respectively shorter and longer than that of ZIS nanosheets. To gain further understanding on this phenomenon, the average emission lifetimes, related to the overall emission decay behaviors of the samples, were also evaluated through the following equation [55]:

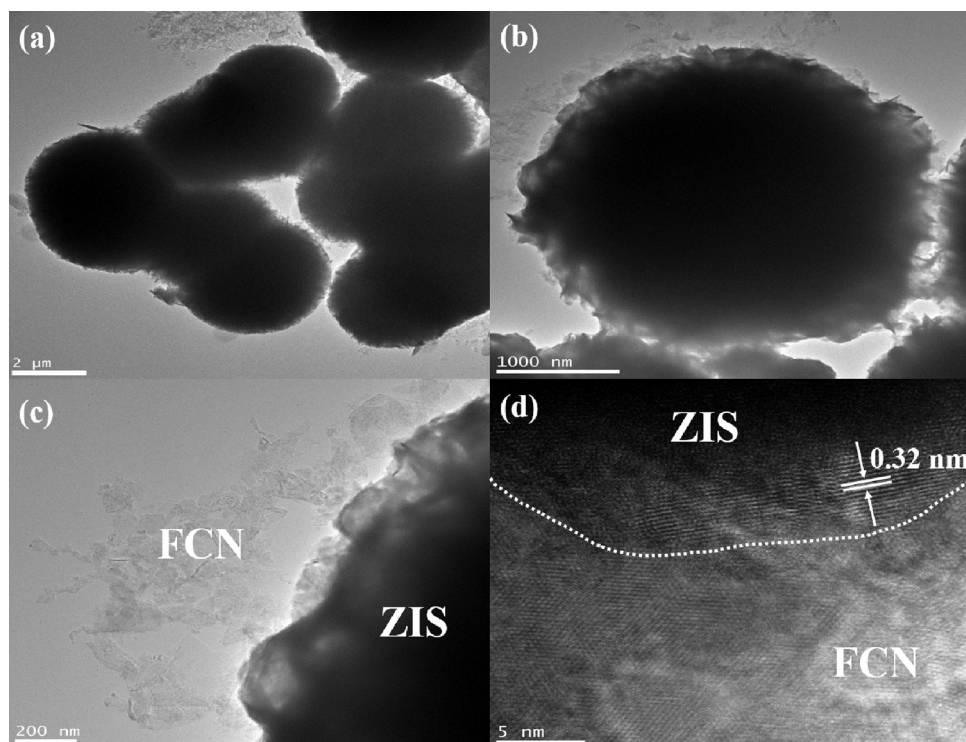


Fig. 3. TEM images of the ZF3 composite.

$$\tau_A = (B_1 \tau_1^2 + B_2 \tau_2^2) / (B_1 \tau_1 + B_2 \tau_2) \quad (2)$$

Using equation (2), the average emission lifetimes of ZIS and ZF3 were 1.1225 ns and 1.5425 ns, respectively, which indicates improved photocatalytic activity of the latter. The longer average lifetime of the ZF3 composite relative to that of ZIS nanosheets suggests that the lifetime of photo-generated charge carriers was prolonged, and a more effective separation of electrons and holes in the ZF3 composite. Hence, the results of the extended lifetime of the photo-induced carriers of the ZF3 composite further illustrate that the introduction of FCN can efficiently retard the recombination of the carriers and thereby enhance the likelihood of the charge carriers participating in photocatalytic degradation.

3.4. Photoelectrochemical response

Photocurrent measurements were performed to evaluate the separation efficiency of photogenerated electron-hole pairs for photocatalytic performance. Fig. 8(a) presents the photocurrent-time curves of FCN, ZIS and ZF composites under visible light irradiation for several on-off cycles. The photocurrent density increased sharply when the light was switched on, and immediately returned to its initial negligible value after the light source was turned off. Notably, the peak values were almost unchanged as the cycles repeated, which indicates that the as-prepared samples exhibited excellent structural stabilities. It is known that the photocurrent is produced by diffusion electrons from the separation of the electron-hole pairs induced by visible light [56]. The ZF3 composite displayed the highest photocurrent, indicating that the ZF3 composite holds stronger ability in generating and transferring the photoexcited charge carrier under light irradiation. In other words, compared with ZIF, the incorporation of FCN on the ZIS surface contributed to the enhancement of separation and transport efficiencies of the photoexcited electron-hole pairs. The electrochemical impedance spectroscopy (EIS) Nyquist plots can further explore the separation efficiency of electron-hole pairs and present the transfer resistance across the solid-liquid junction in the electrode-electrolyte interface region [57,58]. As shown in Fig. 8 (b), the arc radius of the EIS Nyquist plot of

the ZF3 composite was the smallest, indicating that the ZF3 composite possessed the lowest resistance for electron transfer [59]. The electrochemical impedance spectroscopy results are in agreement with that of the photocurrent curves, which collectively indicate that the ZF3 composite possessed the highest separation efficiency of electron-hole and the fastest interfacial electron transfer.

3.5. Photocatalytic performance

3.5.1. Photocatalytic degradation of MO

The photocatalytic activities of as-prepared samples were determined by the degradation of MO under visible light illumination, and results are shown in Fig. 9. Each of the photodegradation reactions was performed after 60 min of adsorption equilibrium in the absence of visible light, and the “blank” curves in Fig. 9(a) represent the absence of any photocatalyst, which indicates negligible degradation of MO. In the presence of photocatalysts, the concentrations of MO decreased much faster for the ZF composites, followed by pure ZIS then FCN (Figs. 9(a)). Pure CN, FCN and ZIS showed limited photocatalytic activity, with MO degradation efficiency of 32%, 44% and 55% after irradiation for 60 min, respectively. The ZF composite photocatalysts showed higher photocatalytic activity than FCN and ZIS, due to the inhibition of the recombination of photogenerated electron-hole pairs. The synergetic effect resulting from hybridizing FCN and ZIS favor the separation of charge carriers, leading to enhanced active species generation and thereby improvement of the photocatalytic degradation of MO. Among the ZF composites, ZF3 exhibited the most efficient degradation, followed by ZF5, ZF1 then ZF8. Specifically, the degradation efficiency increased gradually from 55% to 99% as the FCN content increased from 0 to 30 mg in the ZF composite, and then decreased to 70% as FCN further increased 80 mg. The reason for this non-monotonic relationship is that the over-abundance of FCN may cause the aggregation of FCN, which lowered the photocatalytic performance [60,61]. The single-exponent decay model was used to describe the degradation of MO:

$$C_t = C_0 e^{-kt}$$

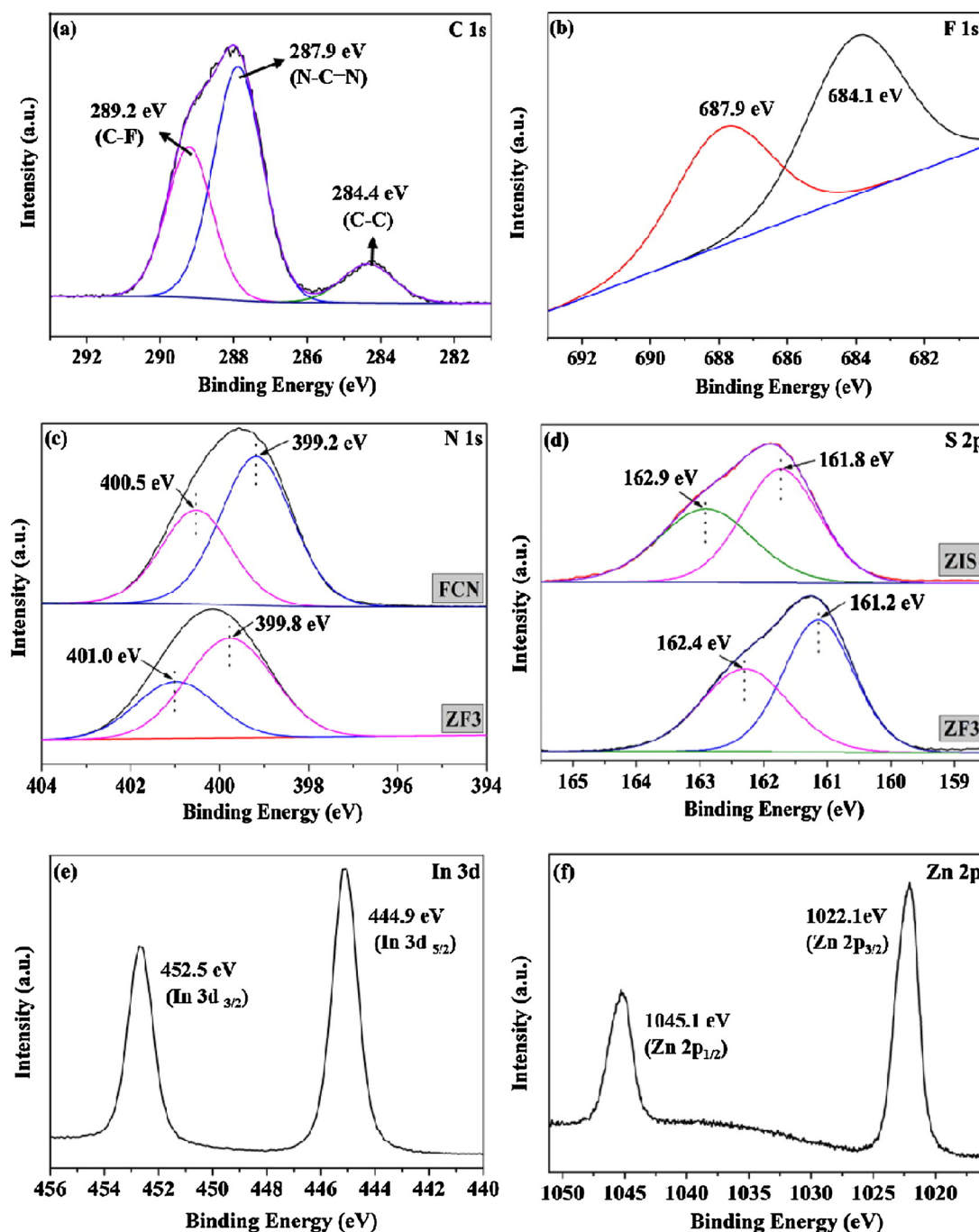


Fig. 4. High-resolution XPS spectra of (a) C 1s region and (b) F 1s region of the ZF3 composite; (c) N 1s region of FCN and ZF3; (d) S 2p region of ZIS and ZF3; (e) In 3d region and (f) Zn 2p region of the ZF3 composite.

where C_t (mg/L) is the concentration of MO at reaction time t (min), C_0 (mg/L) is the initial concentration of MO, and k (min^{-1}) is the rate constant. As shown in Fig. 9(b), the ZF3 composite exhibited the highest rate constant value. Specifically, the degradation rate of MO by FCN, ZIS and ZF3 composite were 0.00996 min^{-1} , 0.01369 min^{-1} and 0.07329 min^{-1} , respectively.

3.5.2. Photocatalytic hydrogen (H_2) generation

To evaluate the photocatalytic performance of the as-prepared photocatalysts, hydrogen evolution experiments from water splitting were carried out under visible light irradiation. Fig. 10(a) shows that the cumulative H_2 increased with time, with that for ZF3 composite increasing the fastest. This indicates that the ZF composite exhibited

improved photocatalytic hydrogen generation activity as compared to the pure constituents. As shown in Fig. 10(a), FCN exhibited higher H_2 production than CN. Meanwhile, ZIS exhibited photocatalytic activity along with H_2 production at $698.2 \mu\text{mol} \cdot \text{g}^{-1}$. After coupling with FCN, the photocatalytic activity of ZIS was significantly enhanced. The H_2 production by ZF composites increased with increasing FCN content, achieving a maximum of $2553.9 \mu\text{mol} \cdot \text{g}^{-1}$ at the FCN content of 30 mg, which is about 3.66 times higher than that of pure ZIS. However, a further increase in the content of FCN led to a decrease in the photocatalytic H_2 production. This decrease is probably due to the following factors: (i) accompanying with the increase of FCN, the relative content of ZIS decreased; and (ii) abundant FCN may turn into a recombination center of photoinduced charges (this has been confirmed by the

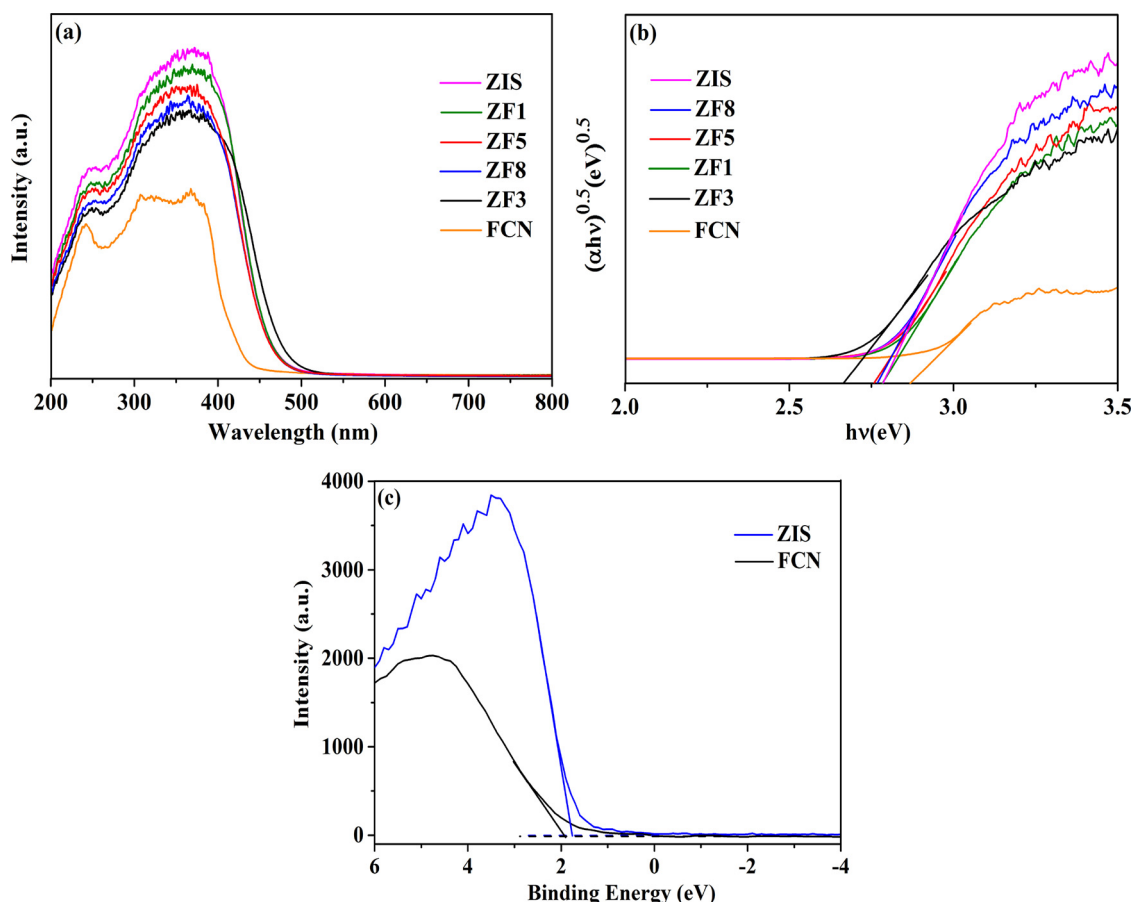


Fig. 5. (a) UV-vis diffuse reflectance spectra and (b) plot of $(\alpha h\nu)^{0.5}$ vs. $h\nu$ (photon energy) of FCN, ZIS, and ZF1, ZF3, ZF5 and ZF8 composites; (c) valence-band XPS spectra of FCN, ZIS and ZF3 composite.

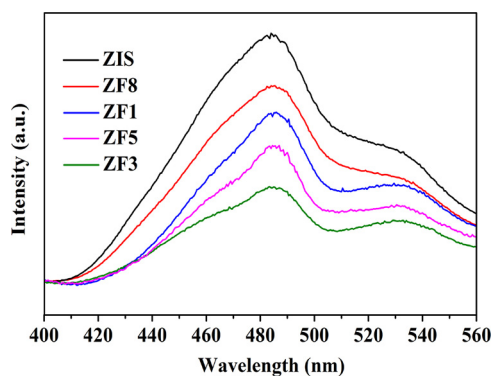


Fig. 6. Photoluminescence (PL) spectra of pure ZIS and the ZF composites at an excitation wavelength of 325 nm.

photoluminescence measurement shown in Fig. 6(a)), which will cause reduction of photocatalytic activity. Therefore, an appropriate FCN amount is important to achieve the optimal H_2 production by the ZF composites. Fig. 10(b) further quantifies the average H_2 production rates of the as-obtained samples as 68.725, 139.64 and 510.778 $\mu\text{mol}\cdot\text{h}^{-1}\cdot\text{g}^{-1}$ for FCN, ZIS and ZF3, respectively. These results indicate that the hydrogen production rates of ZF3 were significantly enhanced by the coupling of FCN with ZIS nanosheets, because of the heterojunctions generated at the interface.

3.6. Photocatalytic mechanism

To investigate the reaction process and the electron transfer

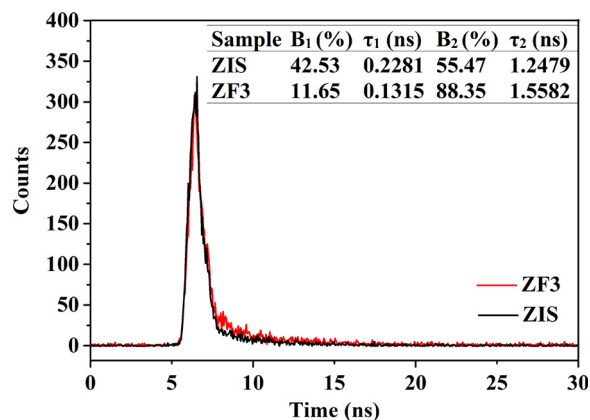


Fig. 7. Fluorescence lifetime obtained from pure ZIS and the ZF3 composite excited by 325 nm at room temperature.

mechanism in this reaction system, the roles of three common active oxidant species, hydroxyl radical ($\cdot\text{OH}$), hole (h^+) and superoxide radical ($\cdot\text{O}_2^-$) have been studied. Herein, disodium ethylenediaminetetraacetate (EDTA), p-benzoquinone (BQ), and tert-Butanol (TBA) were employed as the scavengers of holes (h^+), $\cdot\text{O}_2^-$ and $\cdot\text{OH}$, respectively [62,63]. Fig. 11(a) shows the degradation of MO by the ZF3 composite with time in the absence of any quencher and the presence of each of the three quenchers. As depicted in Fig. 11(a), it can be seen that a significant loss of the degradation rate could be found with the addition of EDTA or BQ, which implies that $\cdot\text{O}_2^-$ and h^+ were the dominant species in the degradation of MO. Furthermore, a little

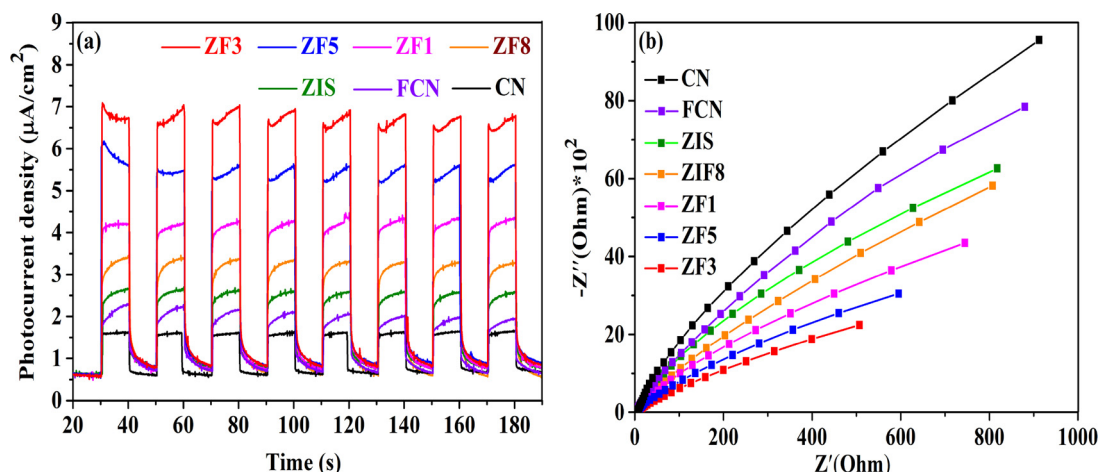


Fig. 8. (a) Transient photocurrent response and (b) EIS Nyquist plots of FCN, ZIS and ZF composites under intermittent visible light irradiation.

inhibition is shown by TBA, indicating that $\cdot\text{OH}$ also contributes to the degradation of MO. On the basis of these results, it is clear to conclude that $\cdot\text{O}_2^-$ and h^+ played a major role in the MO degradation in the reaction system, and $\cdot\text{OH}$ also influenced the MO removal efficiency.

The electron spin resonance (ESR) technique with DMPO was carried out to examine the reactive species that were generated during the ZF3 composite photocatalytic process. The experiments were carried out both under dark and visible light irradiation conditions. As indicated in Fig. 11(b), no signals appeared under dark conditions, and the peak intensities increased with irradiation duration. Specifically, four characteristic peaks and four corresponding troughs of DMPO- $\cdot\text{O}_2^-$ were obtained when the light was on, indicating that $\cdot\text{O}_2^-$ was produced during the photodegradation process. Furthermore, the intensities of the peaks of the spin-trapped TEMPO- h^+ increased when exposed to visible light irradiation relative to that in the dark for the ZF3 composite (Fig. 11(c)). The characteristic signals at g-values (i.e., the spectral splitting factor) of 2.002 was also detected for the ZF3 composite, providing evidence of sulfur vacancies located at the surface [64]. As shown in Fig. 11(d), the intensities of the DMPO- $\cdot\text{OH}$ adducts were negligible in the dark, but the absolute peak and trough values became greater with longer durations of visible light irradiation, demonstrating that $\cdot\text{OH}$ also played an important role in the photocatalytic process. Hence, the radicals trap experiments and ESR analysis reveal that the photocatalytic process was governed by the combined effects of $\cdot\text{O}_2^-$, h^+ and $\cdot\text{OH}$.

The photocatalytic degradation mechanism by the ZF3 composite via the transfer of charge carrier and the formation of oxidizing radical

species is schematically proposed in Fig. 12. Considering the energy band structure of the heterojunction, the photoexcited electrons on the CB of ZIS can rapidly transfer to the CB of FCN, while the photo-generated holes on the VB of FCN can migrate to the VB of ZIS. After the transfer of the photogenerated electrons from the CB of exfoliated ZIS to the CB of FCN, the accumulated electrons with a negative potential of -0.95 eV can oxidize the dissolved oxygen adsorbed onto the surface of FCN to yield $\cdot\text{O}_2^-$ ($E_{\text{O}_2/\cdot\text{O}_2^-} = -0.046\text{ eV}$) and subsequently produce $\cdot\text{OH}$. The resulting reactive species (namely, $\cdot\text{OH}$ and $\cdot\text{O}_2^-$) can efficiently degrade the pollutants. Meanwhile, the strongly oxidized holes, transferred to the VB of ZIS, can directly degrade the MO molecules on the surface of ZIS. The oxidizing species have been clearly confirmed by the ESR signals and trapping experiments (Fig. 11).

The tentative mechanism proposed for the improvement of the photocatalytic H_2 evolution performance of ZF3 photocatalyst is also illustrated in Fig. 12. Under visible light irradiation, both ZIS and FCN could be excited, and the formed staggered band gap promotes the electrons migration to FCN and the holes transfer to ZIS. The photo-generated electrons are captured by H^+ from H_2O to produce H_2 , and the photogenerated holes are trapped by SO_3^{2-} to form SO_4^{2-} in the photocatalytic process. The type-II electron transfer mechanism are of benefit to the separation of charges and electron utilization, which is responsible for the significantly enhanced photocatalytic H_2 production activity of the ZF3 composite relative to pure ZIS.

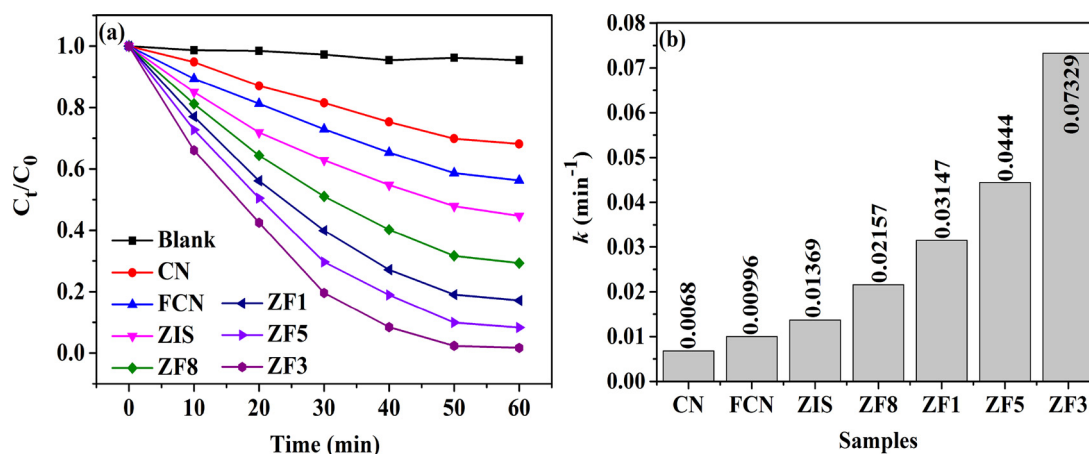


Fig. 9. Photocatalytic MO degradation performance with respect to time (a) and degradation rate constants of MO based on pseudo-first order kinetics (b).

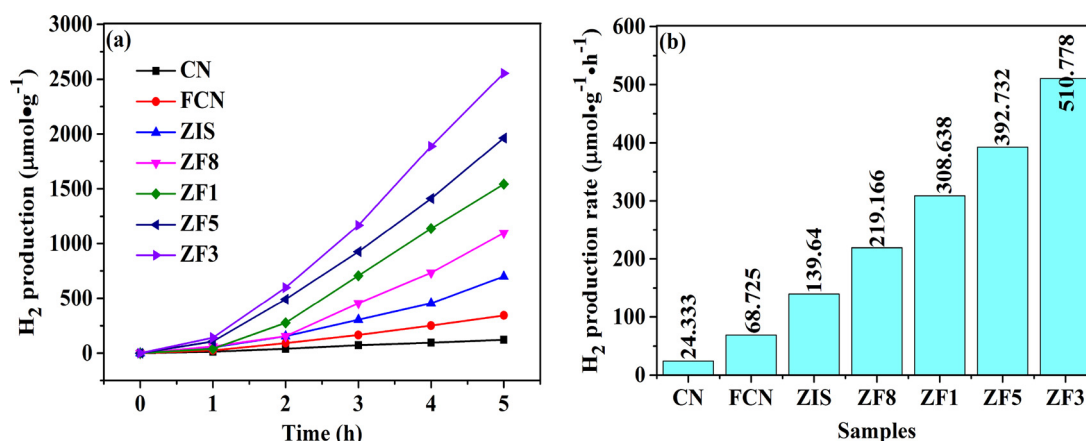


Fig. 10. Visible-light photocatalytic H₂ evolution of FCN, ZIS and ZF composites: (a) cumulative amount of H₂ with time; and (b) H₂ evolution rate.

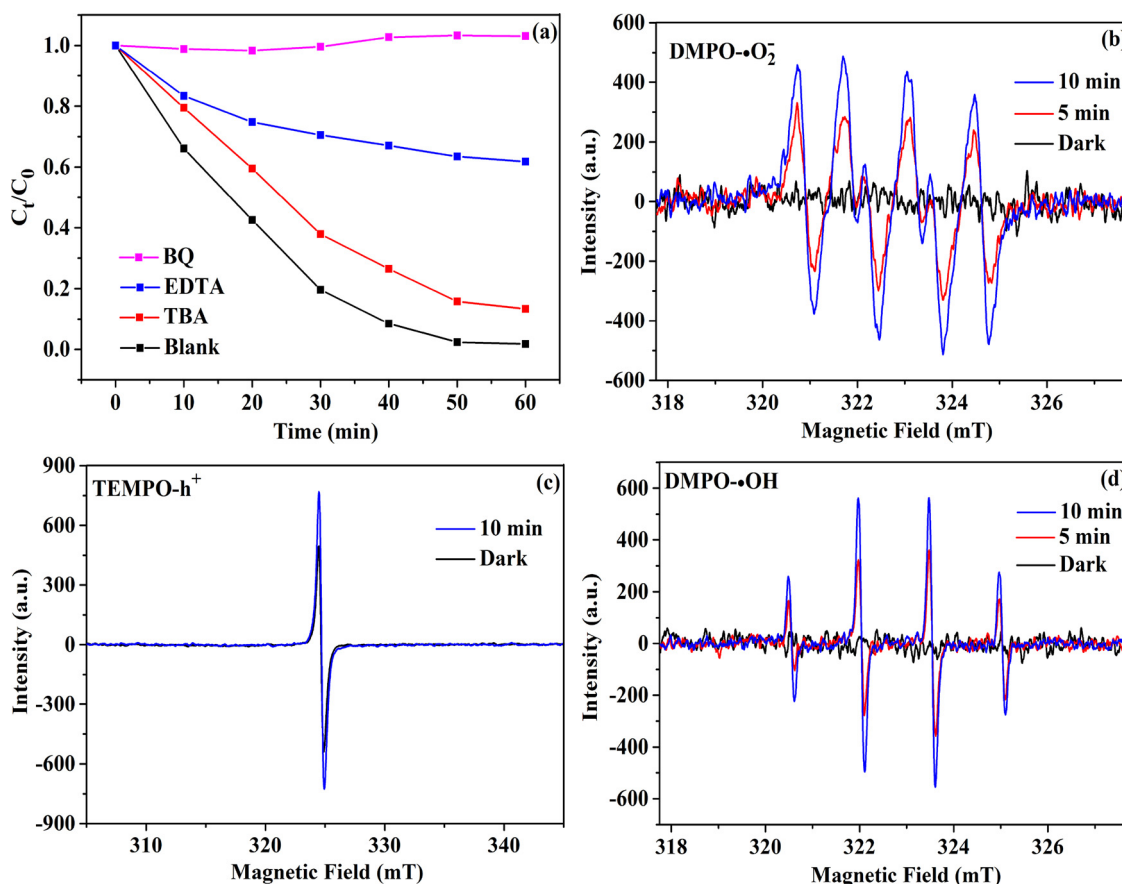


Fig. 11. (a) Effects of different reactive species scavengers on the photo-degradation of MO by the ZF3 composite under visible-light irradiation; ESR spectra of radical adducts trapped by DMPO ($\cdot\text{O}_2^-$ and $\cdot\text{OH}$) and TEMPO (h^+) either in the dark or under visible light irradiation: (b) in methanol dispersion for DMPO- $\cdot\text{O}_2^-$ of ZF3; (c) in aqueous dispersion for TEMPO- h^+ of ZF3; and (d) in aqueous dispersion for DMPO- $\cdot\text{OH}$ of ZF3.

3.7. Recyclability and stability

Other than photocatalytic efficiency, the stability of the photocatalysts for recovery and reuse is also an important factor to measure the quality of the catalysts. Accordingly, the stability of the best-performing ZF3 composite was investigated by repeatedly photodegrading MO over five cycles under the same conditions. Specifically, after every 60 min of photodegradation (i.e., one cycle), the photocatalysts were centrifuged, washed with ethanol and distilled water, and then dried. Fig. 13(a) shows only a 15% drop in the efficiency of MO degradation results by the ZF3 composite after five cycles, the drop of which was at

least in part due to the loss of photocatalysts during the centrifugation and washing steps. Therefore, the results indicate that the ZF3 composite was relatively photo-stable throughout the photocatalytic process. In addition, the XRD spectra of the ZF3 composite before and after the five cycles of degradation was also obtained, as shown in Fig. 13(b). No obvious differences in the XRD patterns are observed, demonstrating a very stable crystal structure even after the repeated degradations. The above analysis indicates that the ZF3 composite presented both outstanding photocatalytic activity and structural stability, which makes it a promising candidate for potential application in environmental remediation and sustainable energy conversion.

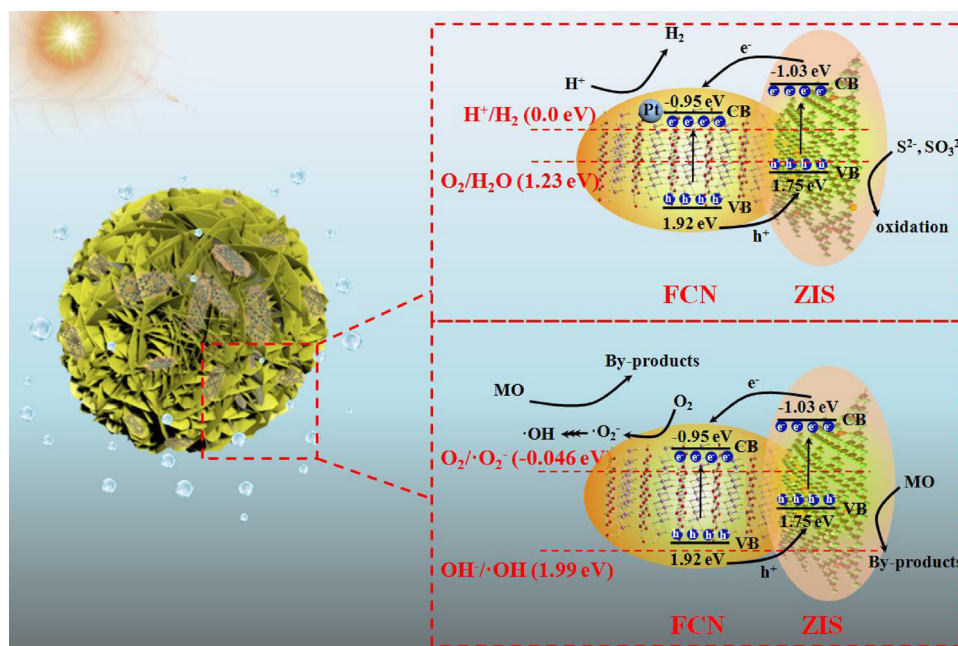


Fig. 12. The mechanism of electrons/holes transfer and separation process of the ZF3 composite under visible light irradiation.

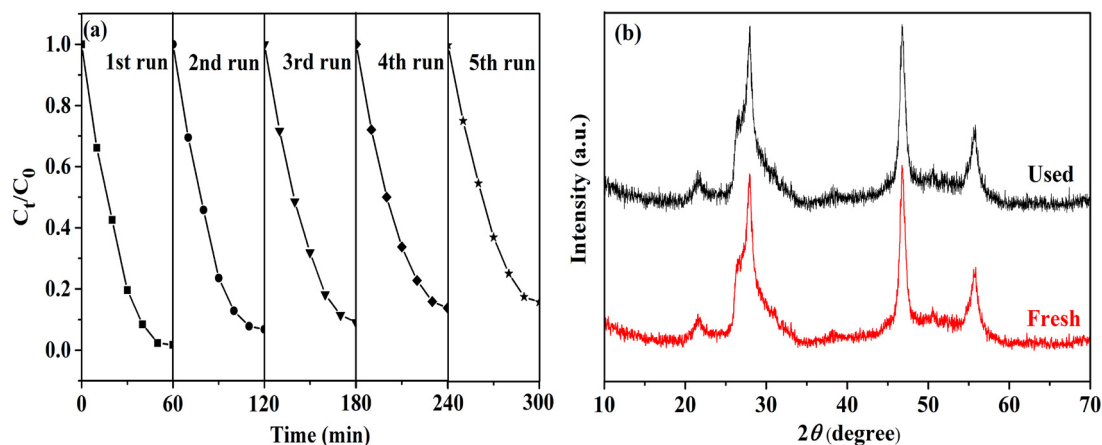


Fig. 13. (a) Photocatalytic degradation of MO by the ZF3 composite under visible-light irradiation over 5 cycles; (b) XRD patterns of the ZF3 composite before and after 5 cycles of photocatalytic MO degradation.

4. Conclusions

In summary, hierarchical 2D-2D $\text{Zn}_3\text{In}_2\text{S}_6/\text{FCN}$ heterojunction nanosheets with various contents of FCN have been successfully synthesized through in-situ growth of FCN nanosheets into $\text{Zn}_3\text{In}_2\text{S}_6$ nanosheets. The resulting 2D/2D heterojunction can provide plentiful charge transfer channels in the ZF composites, which means that the photogenerated charges could migrate along the ZIS nanosheet to the 2D/2D heterojunction interface then to FCN nanosheet. This process contributes to fairly high photoinduced charge separation and migration efficiency, ultimately resulting in remarkably enhanced visible-light-driven photocatalytic activity. Specifically, the best-performing as-synthesized $\text{Zn}_3\text{In}_2\text{S}_6/\text{FCN}$ composite (i.e., namely, the ZF3 composite) exhibited (i) enhanced visible-light-driven photocatalytic MO degradation efficiency that was about 7.36 and 5.35 times higher than those of FCN and $\text{Zn}_3\text{In}_2\text{S}_6$, respectively; and (ii) more efficient visible-light photocatalytic H_2 generation ($2553.9 \mu\text{mol g}^{-1}$) that was significantly enhanced by 3.66 times with respect to $\text{Zn}_3\text{In}_2\text{S}_6$ ($698.2 \mu\text{mol g}^{-1}$). In addition, cycling experiments indicate good photostability and thereby the composites synthesized are promising for

long-term photocatalytic applications. Therefore, this study provides a promising strategy to develop a new generation of hierarchical heterostructure photocatalysts for highly efficient solar-to-fuels conversion and environmental remediation.

Acknowledgments

The authors gratefully acknowledge the funding from the Singapore Ministry of Education Academic Research Funds Tier 2 (MOE2014-T2-2-074; ARC16/15) and Tier 1 (2015-T1-001-023; RG7/15), the GSK (GlaxoSmithKline) – EDB (Economic Development Board) Trust Fund, and the Joint Singapore-Germany Research Project Fund (SGP-PROG3-019).

References

- [1] H. Wang, X.Z. Yuan, Y. Wu, G.M. Zeng, H.R. Dong, X.H. Chen, L.J. Leng, Z.B. Wu, L.J. Peng, *Appl. Catal. B: Environ.* 186 (2016) 19–29.
- [2] L. Xu, C. Srinivasakannan, J.H. Peng, L.B. Zhang, D. Zhang, *J. Alloy. Compd.* 695 (2017) 263–269.
- [3] H. Wang, X.Z. Yuan, Y. Wu, G.M. Zeng, X.H. Chen, L.J. Leng, Z.B. Wu, L.B. Jiang, H. Li, *J. Hazard. Mater.* 286 (2015) 187–194.

- [4] S.H. Shen, L. Zhao, L.J. Guo, *Int. J. Hydrog. Energy* 35 (2010) 10148–10154.
- [5] L. Shang, C. Zhou, T. Bian, H.J. Yu, L.Z. Wu, C.H. Tung, T.R. Zhang, *J. Mater. Chem. A* 1 (2013) 4552–4558.
- [6] X.C. Jiao, Z.W. Chen, X.D. Li†, Y.F. Sun, S. Gao, W.S. Yan, C.M. Wang, Q. Zhang, Y. Lin, Y. Luo, Y. Xie, *J. Am. Chem. Soc.* 139 (2017) 7586–7594.
- [7] W.L. Yang, L. Zhang, J.F. Xie, X.D. Zhang, Q.H. Liu, T. Yao, S.Q. Wei, Q. Zhang, Y. Xie, *Angew. Chem. Int. Ed.* 55 (2016) 6716–6720.
- [8] L. Shi, P.Q. Yin, Y.M. Dai, *Langmuir* 29 (2013) 12818–12822.
- [9] Z.Y. Zhang, K.C. Liu, Z.Q. Feng, Y.N. Bao, B. Dong, *Sci. Rep.* 6 (2016) 19221–19230.
- [10] P.X. Qiu, J.H. Yao, H. Chen, F. Jiang, X.C. Xie, *J. Hazard. Mater.* 317 (2016) 158–168.
- [11] H. Liu, J. Zhang, D. Ao, *Appl. Catal. B: Environ.* 221 (2018) 433–442.
- [12] I. Poulos, N. Papadopoulos, *Sol. Energy Mater.* 20 (1990) 43–51.
- [13] J. Song, C. Ma, W. Zhang, S. Yang, S. Wang, L. Lv, L. Zhu, R. Xia, X. Xu, *J. Mater. Chem. B* 4 (2016) 7909–7918.
- [14] J.H. Zhang, S.G. Meng, X.J. Ye, C.C. Ling, S.J. Zhang, X.L. Fu, S.F. Chen, *Appl. Catal. B: Environ.* 218 (2017) 420–429.
- [15] X. Wang, K. Maeda, A. Thomas, K. Takanabe, G. Xin, J.M. Carlsson, K. Domen, M. Antonietti, *Nat. Mater.* 8 (2009) 76–80.
- [16] W.J. Ong, L.L. Tan, Y.H. Ng, S.T. Yong, S.P. Chai, *Chem. Rev.* 116 (2016) 7159–7329.
- [17] Z. Zhao, Y. Sun, F. Dong, *Nanoscale* 7 (2015) 15–37.
- [18] S.M. Lam, J.C. Sin, A.R. Mohamed, *Mater. Sci. Semicond. Process.* 47 (2016) 62–84.
- [19] L.B. Jiang, X.Z. Yuan, Y. Pan, J. Liang, G.M. Zeng, Z.B. Wu, H. Wang, *Appl. Catal. B: Environ.* 217 (2017) 388–406.
- [20] Y.J. Zhang, T. Mori, J.H. Ye, M. Antonietti, *J. Am. Chem. Soc.* 132 (2010) 6294.
- [21] G.D. Ding, W.T. Wang, T. Jiang, B.X. Han, H.L. Fan, G.Y. Yang, *ChemCatChem* 5 (2013) 192–200.
- [22] B. Chai, J. Yan, C. Wang, Z. Ren, Y. Zhu, *Appl. Surf. Sci.* 391 (2017) 376–383.
- [23] N. Sagara, S. Kamimura, T. Tsubota, T. Ohno, *Appl. Catal. B: Environ.* 192 (2016) 193–198.
- [24] Y. Li, S. Wu, L. Huang, J. Wang, H. Xu, H. Li, *Mater. Lett.* 137 (2014) 281–284.
- [25] S. Guo, Y. Zhu, Y. Yan, Y. Min, J. Fan, Q. Xu, *Appl. Catal. B: Environ.* 185 (2016) 315–321.
- [26] K. Wang, Q. Li, B. Liu, B. Cheng, W. Ho, J. Yu, *Appl. Catal. B: Environ.* 176–177 (2015) 44–52.
- [27] Q. Fan, J. Liu, Y. Yu, S. Zuo, B. Li, *Appl. Surf. Sci.* 391 (2017) 360–368.
- [28] L.B. Jiang, X.Z. Yuan, G.M. Zeng, X.H. Chen, Z.B. Wu, J. Liang, J. Zhang, H. Wang, *ACS Sustainable Chem. Eng.* 5 (2017) 5831–5841.
- [29] Y. Wang, Y. Di, M. s Antonietti, H.R. Li, X.F. Chen, X.C. Wang, *Chem. Mater.* 22 (2010) 5119–5121.
- [30] F.K. Ma, C.L. Sun, Y.L. Shao, Y.Z. Wu, B.B. Huang, X.P. Hao, *New J. Chem.* 41 (2017) 3061–3067.
- [31] Y. Zhang, M. Park, H.-Y. Kim, S.J. Park, *J. Alloys Comp.* 686 (2016) 106–114.
- [32] F.K. Kessler, Y. Zheng, D. Schwarz, C. Merschjann, W. Schnick, X.C. Wang, M.J. Bojdys, *Nat. Rev. Mater.* 2 (2017) 17030–17016.
- [33] Q. Han, B. Wang, J. Gao, Z. Cheng, Y. Zhao, Z. Zhang, L. Qu, *ACS Nano* 10 (2016) 2745–2751.
- [34] P.X. Qiu, J.H. Yao, H. Chen, F. Jiang, X.C. Xie, *J. Hazard. Mater.* 317 (2016) 158–168.
- [35] Y. Wang, X. Wang, M. Antonietti, *Angew. Chem. Int. Ed.* 51 (2012) 68–89.
- [36] A. Vinu, *Adv. Funct. Mater.* 18 (2008) 816–827.
- [37] V. Mazanek, O. Jankovsky, J. Luxa, D. Sedmidubsky, Z. Janousek, F. Sembera, M. Mikulics, Z. Sofer, *Nanoscale* 7 (2015) 13646–13655.
- [38] C. Struzzi, M. Scardamaglia, N. Reckinger, J.F. Colomer, H. Sezen, M. Amati, L. Gregoratti, R. Snyders, C. Bittencourt, *Nano Res.* 9 (2017) 3151–3163.
- [39] C. Struzzia, H. Sezen, M. Amati, L. Gregoratti, N. Reckinger, J.F. Colomer, R. Snyders, C. Bittencourt, M. Scardamaglia, *Appl. Surf. Sci.* 422 (2017) 104–110.
- [40] S. Cao, J. Low, J. Yu, M. Jaroniec, *Adv. Mater.* 27 (2015) 2150–2176.
- [41] Z. Zhang, J. Huang, M. Zhang, Q. Yuan, B. Dong, *Appl. Catal. B: Environ.* 163 (2015) 298–305.
- [42] Z. Chen, Y.J. Xu, *ACS Appl. Mater. Interfaces* 5 (2013) 13353–13363.
- [43] Z. Zhang, J. Huang, M. Zhang, Q. Yuan, B. Dong, *Appl. Catal. B* 163 (2015) 298–305.
- [44] C.W. Tan, G.Q. Zhu, M. Hojamberdiev, K.S. Lokesh, X.C. Luo, L. Jin, J.P. Zhou, P. Liu, *J. Hazard. Mater.* 278 (2014) 572–583.
- [45] L. Yuan, M.Q. Yang, Y.J. Xu, *J. Mater. Chem. A* 2 (2014) 14401–14412.
- [46] Q. Liu, H. Lu, Z.W. Shi, F.L. Wu, J. Guo, K.M. Deng, L. Li, *ACS Appl. Mater. Interfaces* 6 (2014) 17200–17207.
- [47] S. Sakthivel, H. Kisch, *Angew. Chem. Int. Ed.* 42 (2003) 4908–4911.
- [48] A.V. Manole, M. Dobromir, R. Apetrei, V. Nica, D. Luca, *Ceram. Int.* 40 (2014) 9989–9995.
- [49] L.H. Lin, H.H. Ou, Y.F. Zhang, X.C. Wang, *ACS Catal.* 6 (2016) 3921–3931.
- [50] Y. Wu, H. Wang, W.G. Tu, Y. Liu, Y.Z. Tan, X.Z. Yuan, J.W. Chew, *J. Hazard. Mater.* 347 (2018) 412–422.
- [51] Y. Wu, H. Wang, W.G. Tu, S.Y. Wu, Y. Liu, Y.Z. Tan, H.J. Luo, X.Z. Yuan, J.W. Chew, *Appl. Catal. B: Environ.* 229 (2018) 181–191.
- [52] X.T. Wang, C.H. Liow, A. Bisht, X.F. Liu, T.C. Sum, X.D. Chen, S. Zhou, *Adv. Mater.* 27 (2015) 2207–2214.
- [53] Z. Zhang, J. Huang, M. Zhang, Q. Yuan, B. Dong, *Appl. Catal. B* 163 (2015) 298–305.
- [54] S.W. Cao, X.F. Liu, Y.P. Yuan, Z.Y. Zhang, Y.S. Liao, J. Fang, S.C.J. Loo, T.C. Sum, C. Xue, *Appl. Catal. B* 147 (2014) 940–946.
- [55] Y.C. Chen, Y.C. Pu, Y.J. Hsu, *J. Phys. Chem. C* 116 (2012) 2967–2975.
- [56] H.W. Han, X.Z. Zhao, J. Liu, *J. Electrochem. Soc.* 152 (2005) A164–A166.
- [57] (a) N. Li, G. Liu, C. Zhen, F. Li, L.L. Zhang, H.M. Cheng, *Adv. Funct. Mater.* 21 (2011) 1717–1722.
- [58] Z. Hosseini, N. Taghavinia, N. Sharifi, M. Chavoshi, M. Rahman, *J. Phys. Chem. C* 112 (2008) 18686–18689.
- [59] X.Y. Zhang, H.X. Zhang, Y.Y. Xiang, S.B. Hao, Y.X. Zhang, R.N. Guo, X.W. Cheng, M.Z. Xie, Q.F. Cheng, B. Li, *J. Hazard. Mater.* 342 (2018) 353–363.
- [60] Y.Y. Li, J.P. Liu, X.T. Huang, J.G. Yu, *Dalton Trans.* 39 (2010) 3420–3425.
- [61] Y. Hu, X.H. Gao, L. Yu, Y.R. Wang, J.Q. Ning, S.J. Xu, X.W. Lou, *Angew. Chem. Int. Ed.* 52 (2013) 5636–5639.
- [62] H. Wang, X.Z. Yuan, Y. Wu, G.M. Zeng, W.G. Tu, C. Sheng, Y.C. Deng, F. Chen, J.W. Chew, *Appl. Catal. B: Environ.* 209 (2017) 543–553.
- [63] Y. Wu, H. Wang, Y.M. Sun, T. Xiao, W.G. Tu, X.Z. Yuan, G.M. Zeng, S.Z. Li, J.W. Chew, *Appl. Catal. B: Environ.* 227 (2018) 530–540.
- [64] J.G. Wang, Y.J. Chen, W. Zhou, G.H. Tian, Y.T. Xiao, H.Y. Fu, H.G. Fu, *J. Mater. Chem. A* 5 (2017) 8451–8460.